







Quantum motion of a squeezed mechanical oscillator attained via an optomechanical experiment

P. Vezio ¹, A. Chowdhury,² M. Bonaldi ^{3,4}, A. Borrielli,^{3,4} F. Marino ^{5,2}, B. Morana,^{3,6}
G. A. Prodi ^{4,7}, P. M. Sarro,⁶ E. Serra ^{4,6} and F. Marin ^{2,1,5,8,*}

¹*European Laboratory for Non-linear Spectroscopy (LENS), Via Carrara 1, I-50019 Sesto Fiorentino (FI), Italy*

²*CNR-INO, Largo Enrico Fermi 6, I-50125 Firenze, Italy*

³*Institute of Materials for Electronics and Magnetism, Nanoscience-Trento-FBK Division, 38123 Povo, Trento, Italy*

⁴*Istituto Nazionale di Fisica Nucleare (INFN), Trento Institute for Fundamental Physics and Application, I-38123 Povo, Trento, Italy*

⁵*INFN, Sezione di Firenze, Via Sansone 1, I-50019, Sesto Fiorentino (FI), Italy*

⁶*Department of Microelectronics and Computer Engineering /ECTM/DIMES, Delft University of Technology,
Feldmanweg 17, 2628 CT Delft, The Netherlands*

⁷*Dipartimento di Matematica, Università di Trento, I-38123 Povo, Trento, Italy*

⁸*Dipartimento di Fisica e Astronomia, Università di Firenze, Via Sansone 1, I-50019 Sesto Fiorentino (FI), Italy*



(Received 23 June 2020; accepted 13 October 2020; published 5 November 2020)

We experimentally investigate a mechanical squeezed state realized in a parametrically modulated membrane resonator embedded in an optical cavity. We demonstrate that a quantum characteristic of the squeezed dynamics can be revealed and quantified even in a moderately warm oscillator, through the analysis of motional sidebands. We provide a theoretical framework for quantitatively interpreting the observations and present an extended comparison with the experiment. A notable result is that the spectral shape of each motional sideband provides a clear signature of a quantum mechanical squeezed state without the necessity of absolute calibrations, in particular in the regime where residual fluctuations in the squeezed quadrature are reduced below the zero-point level.

DOI: [10.1103/PhysRevA.102.053505](https://doi.org/10.1103/PhysRevA.102.053505)

I. INTRODUCTION

Quantum mechanics has proven to be very effective in describing the behavior of physical systems at the atomic and subatomic levels and a large part of our technology is based on quantum processes occurring on microscopic scales. Since the inception of the theory, a long debate has continued about which typically quantum properties are conserved or modified at the quantum-to-classical boundary and, eventually, observed in the macroscopic reality. While an extensive literature exists on nonclassical properties of molecules, atoms, and their constituents, experiments demonstrating genuine quantum properties of macroscopic degrees of freedom are comparatively very few. This situation has greatly changed in the past years thanks to the progresses in the realization and control of cavity optomechanical systems, in which the radiation pressure coupling between optical and mechanical modes allows us to manipulate their state at the quantum level [1].

One major result of the field is the cooling of macroscopic oscillators close to their quantum ground state [2–4] and the observation of quantum signatures in their motion. One of such nonclassical features is the so-called motional sideband asymmetry. The mechanical interaction of the oscillator with a probe electromagnetic field measuring interferometrically its position, produces in the latter two motional sidebands at $\pm\Omega_m$ around its main optical frequency [4–10], where Ω_m

is the mechanical eigenfrequency. The asymmetry originates from the fact that a mechanical oscillator in the quantum ground state can only absorb energy. Since the blue sideband can be associated to an anti-Stokes scattering, implying an energy transfer from the oscillator to the field (absorption of a phonon and frequency up-conversion of a photon), and vice versa for the red (Stokes) sideband, even at finite temperature the former process is less probable. The spectral areas below the blue and red sidebands are proportional to \bar{n}_{th} and $\bar{n}_{th} + 1$ respectively, where \bar{n}_{th} is the mean thermal occupation number. In cavity optomechanical systems, the interplay between radiation pressure force acting on the oscillator and the delay in the intracavity field buildup generates an additional mechanical damping, allowing the effective cooling of the mechanical motion to a lower mean phonon number \bar{n} [1]. The ratio between Stokes and anti-Stokes sidebands can be written as $R_0 = (\bar{n} + 1)/\bar{n}$ and a deviation from unity of R_0 becomes measurable for sufficiently low \bar{n} . Such an imbalance provides a direct measure of the displacement noise associated with zero-point quantum fluctuations [11–13] and allows for a direct calibration of the mean phonon occupation number, i.e., of the absolute temperature of the oscillator [14–16].

The preparation of strongly nonclassical states in such systems and the identification of specific quantum indicators would represent a relevant step further, from both the scientific and technological points of view. Recent microwave experiments with cooled nano-oscillators have produced a mechanical squeezed state where the fluctuations in one quadrature are reduced below the zero-point level [17–20].

*marin@fi.infn.it

Such a noise reduction can actually play an important role in several applications, for instance in optimizing the sensitivity of the oscillator used as quantum sensor. Nevertheless, the quadrature spectra do not carry any distinctive feature of the nonclassical nature of the phenomenon, which can be only inferred (and actually demonstrated) *a posteriori* through accurate calibration procedures.

In a recent experiment, we realized a squeezed state of a macroscopic mechanical oscillator embedded in an optical cavity [21]. The squeezing is generated via parametric modulation of the oscillator spring constant at twice its resonance frequency [22]. In this condition, classical and quantum fluctuations in phase with the parametric driving are amplified, while those 90 degrees out of phase are suppressed. As a result, the oscillator motion in the phase space is squeezed in one quadrature and amplified in the orthogonal one. Such a scheme had already been implemented in cavity optomechanical experiments with thermal oscillators, where the modulation of the spring constant is achieved by modulating the light frequency or intensity [23,24].

Remarkably, in the presence of parametric modulation, the motional sidebands assume a peculiar shape, related to the modified system dynamics, unveiling the quantum component of the squeezed oscillator motion. Here we further investigate this phenomenon, extending the experimental measurements of Ref. [21] and developing a theoretical framework able to explain the observations.

The paper is organized as follows. In Sec. II, we introduce the theoretical background with a discussion of key concepts and the derivation of relevant equations. In Sec. III, we describe the experimental setup. In Sec. IV, we present the experimental results and compare them with the theoretical predictions. In particular, we report a complete characterization of the sideband asymmetry, as a function of the strength of the parametric drive, occupation number, and detuning of the cooling beam. Our results demonstrate that some degree of quantum squeezing occurs and can be observed and quantified through the analysis of the motional sidebands, even for a moderately cooled mechanical oscillator, in which thermal noise is dominating over quantum fluctuations. We also show theoretically that, when the residual fluctuations in the squeezed quadrature are reduced below the zero-point level, the sideband spectra provide a clear indication of a quantum mechanical squeezed state, without the necessity of absolute calibrations. The conclusions and future perspectives are presented in Sec. V.

II. THEORETICAL BACKGROUND

The linearized evolution equations for the intracavity field operator $\delta\hat{a}$ and the mechanical bosonic operator \hat{b} , in the frame rotating at frequency ω_L , are [1]

$$\delta\dot{\hat{a}} = \left(i\Delta - \frac{\kappa}{2}\right)\delta\hat{a} + ig_0\alpha(\hat{b} + \hat{b}^\dagger) + \sqrt{\kappa}\delta\hat{a}_{\text{in}}, \quad (1)$$

$$\dot{\hat{b}} = \left(-i\Omega_m^0 - \frac{\Gamma_m}{2}\right)\hat{b} + ig_0(\alpha^*\delta\hat{a} + \alpha\delta\hat{a}^\dagger) + \sqrt{\Gamma_m}\hat{b}_{\text{th}}, \quad (2)$$

where $\Delta = \omega_L - \omega_c$ is the detuning with respect to the cavity resonance frequency ω_c , κ , and Γ_m are the optical and mechanical decay rates, Ω_m^0 is the mechanical resonance frequency, g_0 is the single-photon optomechanical coupling rate, and α is the intracavity mean field. The input noise operators are characterized by the correlation functions

$$\langle\hat{a}_{\text{in}}(t)\hat{a}_{\text{in}}^\dagger(t')\rangle = \delta(t-t'), \quad (3)$$

$$\langle\hat{a}_{\text{in}}^\dagger(t)\hat{a}_{\text{in}}(t')\rangle = 0, \quad (4)$$

$$\langle\hat{b}_{\text{th}}(t)\hat{b}_{\text{th}}^\dagger(t')\rangle = (\bar{n}_{\text{th}} + 1)\delta(t-t'), \quad (5)$$

$$\langle\hat{b}_{\text{th}}^\dagger(t)\hat{b}_{\text{th}}(t')\rangle = \bar{n}_{\text{th}}\delta(t-t'), \quad (6)$$

where \bar{n}_{th} is the thermal occupation number.

In our experiment, the input field is composed of two tones, whose frequencies are shifted by $\pm\Omega_m$ around their mean value ω_L . The shift frequency $\Omega_m \simeq \Omega_m^0$ is tuned to the effective mechanical resonance frequency, modified by the optomechanical interaction. It is determined experimentally by observing the oscillator spectrum, while in the framework of this theoretical model it will be defined later in a self-consistent way [Eq. (14)]. The mean value of the input field has the form

$$\alpha_{\text{in}} = \alpha_-^{\text{in}} e^{-i(\omega_L - \Omega_m)t} + \alpha_+^{\text{in}} e^{-i(\omega_L + \Omega_m)t}. \quad (7)$$

The intracavity mean field, in the rotating frame, is $\alpha = \alpha_- e^{i\Omega_m t} + \alpha_+ e^{-i\Omega_m t}$, with amplitudes

$$\alpha_{\pm} = \alpha_{\pm}^{\text{in}} \frac{\sqrt{\kappa_{\text{in}}}}{-i(\Delta \pm \Omega_m) + \kappa/2}, \quad (8)$$

where κ_{in} is the input coupling rate.

In the Fourier space, Eq. (1) can be written as

$$\delta\tilde{a}(\Omega) = \frac{1}{-i\Omega - i\Delta + \kappa/2} \{ig_0[\alpha_-(\tilde{b}(\Omega + \Omega_m) + \tilde{b}^\dagger(\Omega + \Omega_m)) + \alpha_+(\tilde{b}(\Omega - \Omega_m) + \tilde{b}^\dagger(\Omega - \Omega_m))] + \sqrt{\kappa}\delta\tilde{a}_{\text{in}}(\Omega)\}, \quad (9)$$

where we use \tilde{O} to indicate the Fourier transformed of the operator \hat{O} , and \tilde{O}^\dagger for the Fourier transformed of \hat{O}^\dagger , therefore $(\tilde{O}(\Omega))^\dagger = \tilde{O}^\dagger(-\Omega)$.

When Eq. (9) and its Hermitian conjugate are replaced into Eq. (2) in the Fourier space, the mean-field factors α and α^* in the optomechanical coupling shift the $\delta\tilde{a}$ and $\delta\tilde{a}^\dagger$ operators by $\pm\Omega_m$, giving terms proportional to $\tilde{b}(\Omega)$, $\tilde{b}(\Omega \pm 2\Omega_m)$, $\tilde{b}^\dagger(\Omega)$, and $\tilde{b}^\dagger(\Omega \pm 2\Omega_m)$. Equation (2) can thus be written as

$$\begin{aligned} (-i\Omega + i\Omega_m^0 + \Gamma_m/2)\tilde{b}(\Omega) = & -g_0^2[\mathcal{C}_1\tilde{b}(\Omega) + \mathcal{C}_2\tilde{b}(\Omega - 2\Omega_m) \\ & + \mathcal{C}_3\tilde{b}(\Omega + 2\Omega_m) + \mathcal{C}_4\tilde{b}^\dagger(\Omega) + \mathcal{C}_5\tilde{b}^\dagger(\Omega - 2\Omega_m) + \mathcal{C}_6\tilde{b}^\dagger(\Omega + 2\Omega_m)] + \tilde{b}_{\text{in}}(\Omega), \end{aligned} \quad (10)$$

where \mathcal{C}_i are c-numbers and the source term is

$$\begin{aligned} \tilde{b}_{\text{in}}(\Omega) = & \sqrt{\Gamma_m} \tilde{b}_{\text{th}}(\Omega) + ig_0\sqrt{\kappa} \left[\alpha_-^* \frac{\delta\tilde{a}_{\text{in}}(\Omega - \Omega_m)}{-i\Omega - i\Delta + i\Omega_m + \kappa/2} + \alpha_+^* \frac{\delta\tilde{a}_{\text{in}}(\Omega + \Omega_m)}{-i\Omega - i\Delta - i\Omega_m + \kappa/2} \right. \\ & \left. + \alpha_- \frac{\delta\tilde{a}_{\text{in}}^\dagger(\Omega + \Omega_m)}{-i\Omega + i\Delta - i\Omega_m + \kappa/2} + \alpha_+ \frac{\delta\tilde{a}_{\text{in}}^\dagger(\Omega - \Omega_m)}{-i\Omega + i\Delta + i\Omega_m + \kappa/2} \right]. \end{aligned} \tag{11}$$

The total input noise source described by Eq. (11) includes thermal noise and back-action noise, the latter given by the terms into square brackets.

We now restrict our analysis to weak coupling, in which case the optomechanical damping rate and frequency shift of the mechanical oscillator [whose expressions will be given later, in Eqs. (13) and (14)] are much smaller than its resonance frequency. Therefore, in Eq. (10), we just consider the quasiresonant components in the optomechanical coupling term. From the left-hand side of Eq. (10), we see that \tilde{b} is peaked around Ω_m , while \tilde{b}^\dagger is peaked around $-\Omega_m$. Therefore, the relevant terms in the optomechanical coupling, on the right-hand side of Eq. (10), are those proportional to $\tilde{b}(\Omega)$ and $\tilde{b}^\dagger(\Omega - 2\Omega_m)$. Writing the explicit form of the \mathcal{C} coefficients, Eq. (10) becomes

$$\begin{aligned} (-i\Omega + i\Omega_m^0 + \Gamma_m/2)\tilde{b}(\Omega) \simeq & -g_0^2 \left[|\alpha_-|^2 \tilde{b}(\Omega) \left(\frac{1}{-i\Omega - i\Delta + i\Omega_m + \kappa/2} - \frac{1}{-i\Omega + i\Delta - i\Omega_m + \kappa/2} \right) \right. \\ & + |\alpha_+|^2 \tilde{b}(\Omega) \left(\frac{1}{-i\Omega - i\Delta - i\Omega_m + \kappa/2} - \frac{1}{-i\Omega + i\Delta + i\Omega_m + \kappa/2} \right) \\ & \left. + \alpha_-^* \alpha_+ \tilde{b}^\dagger(\Omega - 2\Omega_m) \left(\frac{1}{-i\Omega - i\Delta + i\Omega_m + \kappa/2} - \frac{1}{-i\Omega + i\Delta + i\Omega_m + \kappa/2} \right) \right] + \tilde{b}_{\text{in}}(\Omega). \end{aligned} \tag{12}$$

In the right-hand side of Eq. (12), we notice the usual optomechanical effects of the two laser tones (first two terms inside square brackets), plus their coherent common interaction, proportional to the fields product $\alpha_-^* \alpha_+$, that originates the parametric squeezing. It can be directly calculated that this parametric effect is null for $\Delta = 0$, i.e., when the two tones are equally shifted with respect to the cavity resonance.

The standard optomechanical interaction is parametrized by the total optical damping rate Γ_{opt} , defined as [1]

$$\begin{aligned} \Gamma_{\text{opt}} = & 2g_0^2 \text{Re} \left[|\alpha_-|^2 \left(\frac{1}{-i\Omega - i\Delta + i\Omega_m + \kappa/2} - \frac{1}{-i\Omega + i\Delta - i\Omega_m + \kappa/2} \right) \right. \\ & \left. + |\alpha_+|^2 \left(\frac{1}{-i\Omega - i\Delta - i\Omega_m + \kappa/2} - \frac{1}{-i\Omega + i\Delta + i\Omega_m + \kappa/2} \right) \right], \end{aligned} \tag{13}$$

and by a frequency shift that determines the effective resonance frequency Ω_m according to the equation

$$\begin{aligned} \Omega_m = & \Omega_m^0 + g_0^2 \text{Im} \left[|\alpha_-|^2 \left(\frac{1}{-i\Omega - i\Delta + i\Omega_m + \kappa/2} - \frac{1}{-i\Omega + i\Delta - i\Omega_m + \kappa/2} \right) \right. \\ & \left. + |\alpha_+|^2 \left(\frac{1}{-i\Omega - i\Delta - i\Omega_m + \kappa/2} - \frac{1}{-i\Omega + i\Delta + i\Omega_m + \kappa/2} \right) \right]. \end{aligned} \tag{14}$$

For an easier comparison with the experimental data, it is useful to define the total optomechanical coupling strength $g^2 = g_0^2(|\alpha_-|^2 + |\alpha_+|^2)$ and the the ratio between intracavity powers $\epsilon_c = |\alpha_-|^2/(|\alpha_-|^2 + |\alpha_+|^2)$. Using the quasiresonant frequency condition $\Omega \simeq \Omega_m$, the total damping rate $\Gamma_{\text{eff}} = \Gamma_m + \Gamma_{\text{opt}}$ can be written as

$$\Gamma_{\text{eff}} = \Gamma_m + g^2\kappa \left(\frac{\epsilon_c}{\Delta^2 + \kappa^2/4} - \frac{\epsilon_c}{(\Delta - 2\Omega_m)^2 + \kappa^2/4} + \frac{1 - \epsilon_c}{(\Delta + 2\Omega_m)^2 + \kappa^2/4} - \frac{1 - \epsilon_c}{\Delta^2 + \kappa^2/4} \right). \tag{15}$$

With the same condition and notation, Eq. (12) simplifies to

$$\begin{aligned} & (-i\Omega + i\Omega_m + \Gamma_{\text{eff}}/2)\tilde{b}(\Omega) \\ & = -\frac{\Gamma_{\text{par}}}{2} e^{i\phi} \tilde{b}^\dagger(\Omega - 2\Omega_m) + \tilde{b}_{\text{in}}(\Omega), \end{aligned} \tag{16}$$

where

$$\Gamma_{\text{par}} = \frac{4g^2\sqrt{\epsilon_c(1 - \epsilon_c)}\Delta}{\Delta^2 + \kappa^2/4} \tag{17}$$

and $\phi = \pi/2 + \arg[\alpha_-^* \alpha_+]$.

Moving to the frame rotating at Ω_m by means of the transformation

$$\hat{b}_R = \hat{b} e^{i\Omega_m t}, \quad \hat{b}_R^\dagger = \hat{b}^\dagger e^{-i\Omega_m t} \tag{18}$$

and, for Fourier transformed operators,

$$\tilde{b}_R(\Omega) = \tilde{b}(\Omega + \Omega_m), \quad \tilde{b}_R^\dagger(\Omega) = \tilde{b}^\dagger(\Omega - \Omega_m), \tag{19}$$

and defining the frequency with respect to the mechanical resonance as $\delta\Omega = \Omega - \Omega_m$, Eq. (16) and its Hermitian conjugate can be written in the form of the system of coupled

linear equations

$$\begin{pmatrix} -i\delta\Omega + \frac{\Gamma_{\text{eff}}}{2} & \frac{\Gamma_{\text{par}}}{2} e^{i\phi} \\ \frac{\Gamma_{\text{par}}}{2} e^{-i\phi} & -i\delta\Omega + \frac{\Gamma_{\text{eff}}}{2} \end{pmatrix} \begin{pmatrix} \tilde{b}_R \\ \tilde{b}_R^\dagger \end{pmatrix} = \begin{pmatrix} \tilde{b}_{\text{in}} \\ \tilde{b}_{\text{in}}^\dagger \end{pmatrix}. \quad (20)$$

The determinant of the system matrix is

$$\mathcal{D} = \left(-i\delta\Omega + \frac{\Gamma_+}{2}\right) \left(-i\delta\Omega + \frac{\Gamma_-}{2}\right), \quad (21)$$

where

$$\Gamma_{\pm} = \Gamma_{\text{eff}} \pm \Gamma_{\text{par}} \quad (22)$$

and the solutions of the system can be written as

$$\tilde{b}_R = \frac{1}{\mathcal{D}} \left[\left(-i\delta\Omega + \frac{\Gamma_{\text{eff}}}{2}\right) \tilde{b}_{\text{in}} - \frac{\Gamma_{\text{par}}}{2} e^{i\phi} \tilde{b}_{\text{in}}^\dagger \right], \quad (23)$$

$$\tilde{b}_R^\dagger = \frac{1}{\mathcal{D}} \left[\left(-i\delta\Omega + \frac{\Gamma_{\text{eff}}}{2}\right) \tilde{b}_{\text{in}}^\dagger - \frac{\Gamma_{\text{par}}}{2} e^{-i\phi} \tilde{b}_{\text{in}} \right]. \quad (24)$$

The correlation function for the input noise source of Eq. (11) is obtained from Eqs. (3)–(6) by considering that $\langle \hat{O}(t) \hat{O}^\dagger(t') \rangle = c \delta(t - t')$ implies $\langle \tilde{O}(\Omega) \tilde{O}^\dagger(\Omega') \rangle = 2\pi c \delta(\Omega + \Omega')$:

$$\frac{1}{2\pi} \langle \tilde{b}_{\text{in}}(-\Omega) \tilde{b}_{\text{in}}^\dagger(\Omega) \rangle = \Gamma_{\text{m}}(\bar{n}_{\text{th}} + 1) + A^+, \quad (25)$$

$$\frac{1}{2\pi} \langle \tilde{b}_{\text{in}}^\dagger(-\Omega) \tilde{b}_{\text{in}}(\Omega) \rangle = \Gamma_{\text{m}} \bar{n}_{\text{th}} + A^-, \quad (26)$$

$$\begin{aligned} \frac{1}{2\pi} \langle \tilde{b}_{\text{in}}(-\Omega) \tilde{b}_{\text{in}}(\Omega) \rangle &= \frac{1}{2\pi} \langle \tilde{b}_{\text{in}}^\dagger(-\Omega) \tilde{b}_{\text{in}}^\dagger(\Omega) \rangle^* \\ &= -g_0^2 \kappa \frac{\alpha_-^* \alpha_+}{\Delta^2 + \kappa^2/4}, \end{aligned} \quad (27)$$

where the Stokes and anti-Stokes rates due to the two field tones are [1]

$$A^- = g_0^2 \kappa \left[\frac{|\alpha_-|^2}{\Delta^2 + \kappa^2/4} + \frac{|\alpha_+|^2}{(\Delta + 2\Omega_{\text{m}})^2 + \kappa^2/4} \right], \quad (28)$$

$$A^+ = g_0^2 \kappa \left[\frac{|\alpha_-|^2}{(\Delta - 2\Omega_{\text{m}})^2 + \kappa^2/4} + \frac{|\alpha_+|^2}{\Delta^2 + \kappa^2/4} \right], \quad (29)$$

and it can be verified that $\Gamma_{\text{opt}} = A^- - A^+$.

The spectra of the Stokes and anti-Stokes motional sidebands are finally calculated from Eqs. (23) and (24) using the correlation functions given above, and are respectively

$$\begin{aligned} S_{\tilde{b}_R^\dagger \tilde{b}_R^\dagger} &= \frac{1}{2\pi} \langle \tilde{b}_R(-\delta\Omega) \tilde{b}_R^\dagger(\delta\Omega) \rangle \\ &= \frac{\Gamma_{\text{eff}}}{2} \left[\frac{1 + \bar{n} - s/2}{\delta\Omega^2 + \Gamma_-^2/4} + \frac{1 + \bar{n} + s/2}{\delta\Omega^2 + \Gamma_+^2/4} \right], \end{aligned} \quad (30)$$

$$\begin{aligned} S_{\tilde{b}_R \tilde{b}_R} &= \frac{1}{2\pi} \langle \tilde{b}_R^\dagger(-\delta\Omega) \tilde{b}_R(\delta\Omega) \rangle \\ &= \frac{\Gamma_{\text{eff}}}{2} \left[\frac{\bar{n} + s/2}{\delta\Omega^2 + \Gamma_-^2/4} + \frac{\bar{n} - s/2}{\delta\Omega^2 + \Gamma_+^2/4} \right], \end{aligned} \quad (31)$$

where we have introduced the squeezing parameter $s = \Gamma_{\text{par}}/\Gamma_{\text{eff}}$ and the oscillator effective phonon number in the

absence of parametric effect is

$$\bar{n} = \frac{\Gamma_{\text{m}} \bar{n}_{\text{th}} + \Gamma_{\text{opt}} \bar{n}_{\text{BA}}}{\Gamma_{\text{eff}}} \quad (32)$$

with $\bar{n}_{\text{BA}} = A^+/\Gamma_{\text{opt}}$.

The spectral shape of each motional sideband departs from a simple Lorentzian peak, and it is indeed composed by the sum of two Lorentzian curves with the same center but different amplitudes and widths. The ratios between the areas of the broad and narrow Lorentzian components in the two sidebands are

$$R_+ = \frac{\bar{n} + 1 + s/2}{\bar{n} - s/2}, \quad (33)$$

$$R_- = \frac{\bar{n} + 1 - s/2}{\bar{n} + s/2}, \quad (34)$$

respectively for the broader (R_+) and narrower (R_-) components. In the absence of parametric gain ($s = 0$), the two ratios coincide, and we recover the usual sideband asymmetry result for a thermal state $R_+ = R_- = R_0$.

A generic quadrature X_θ of the oscillator is defined as $X_\theta = (e^{i\theta} \hat{b}_R + e^{-i\theta} \hat{b}_R^\dagger)/2$. The quadrature operator can be calculated in the Fourier space from Eqs. (23) and (24), obtaining

$$\begin{aligned} \tilde{X}_\theta &= \frac{1}{2\mathcal{D}} \left[e^{i\theta} \tilde{b}_{\text{in}} \left(-i\delta\Omega + \frac{\Gamma_{\text{eff}}}{2} - \frac{\Gamma_{\text{par}}}{2} e^{-i(2\theta+\phi)} \right) \right. \\ &\quad \left. + e^{-i\theta} \tilde{b}_{\text{in}}^\dagger \left(-i\delta\Omega + \frac{\Gamma_{\text{eff}}}{2} - \frac{\Gamma_{\text{par}}}{2} e^{i(2\theta+\phi)} \right) \right]. \end{aligned} \quad (35)$$

The shape of the spectrum of X_θ can be written as the sum of two Lorentzian functions, with width Γ_+ and Γ_- . Single Lorentzian shapes characterize the quadratures defined by $(2\theta + \phi) = 0$ and $(2\theta + \phi) = \pi$. These quadratures are defined in the following as $Y \equiv X_{-\phi/2}$ and $X \equiv X_{-\phi/2+\pi/2}$. Their operators are

$$Y = \frac{e^{-i\phi/2} \tilde{b}_{\text{in}} + e^{i\phi/2} \tilde{b}_{\text{in}}^\dagger}{2(-i\delta\Omega + \frac{\Gamma_+}{2})}, \quad X = \frac{i(e^{-i\phi/2} \tilde{b}_{\text{in}} - e^{i\phi/2} \tilde{b}_{\text{in}}^\dagger)}{2(-i\delta\Omega + \frac{\Gamma_-}{2})}, \quad (36)$$

and the associated spectra are

$$S_{YY} = \frac{\Gamma_{\text{eff}}(2\bar{n} + 1)}{4(\delta\Omega^2 + \frac{\Gamma_+^2}{4})}, \quad S_{XX} = \frac{\Gamma_{\text{eff}}(2\bar{n} + 1)}{4(\delta\Omega^2 + \frac{\Gamma_-^2}{4})}. \quad (37)$$

The integrals of the spectra give different variances in the two orthogonal quadratures $\sigma_Y^2 = \sigma_0^2/(1 + s)$ and $\sigma_X^2 = \sigma_0^2/(1 - s)$ with $\sigma_0^2 = (2\bar{n} + 1)/4$. The oscillator is said to be in a squeezed state.

To summarize, in a classical description the motion of the oscillator is described by commuting variables, and the spectra corresponding to the two motional sidebands must be identical. On the other hand, in a quantum-mechanical description, even if the oscillator is dominated by thermal noise (i.e., $\bar{n} \gg 1$), the sideband asymmetry is always present ($R_0 > 1$), being originated by the noncommutativity between its ladder operators. Of course, the effect is actually measurable only for moderately low occupation numbers \bar{n} .

In the presence of parametric modulation, when the system is in a squeezed state, the sideband ratios R_+ and R_- differ not only from unity, but also from the ratio R_0 measured in a

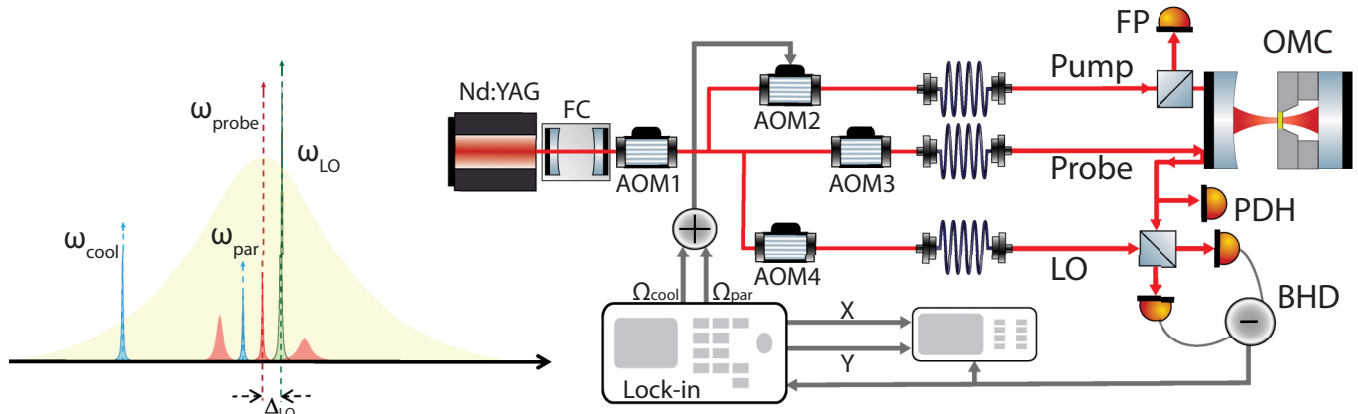


FIG. 1. Sketch of the experimental setup (see text) and conceptual scheme of the field frequencies. The LO is placed on the blue side of the probe (ω_{probe}) and detuned by $\Delta_{\text{LO}} \ll \Omega_m$; therefore, the Stokes lines are on the red side of the LO, while the anti-Stokes lines are on the blue side. In the heterodyne spectra, they are located respectively at $\Omega_m + \Delta_{\text{LO}}$ (Stokes) and $\Omega_m - \Delta_{\text{LO}}$ (anti-Stokes).

thermal state. Namely, the ratio is higher for the broadened Lorentzian component, while for the narrowed component it approaches unity as $s \rightarrow 1$ (i.e., close to the parametric instability threshold).

Therefore, the quantum features of the oscillator motion can be brought out even for a state having a variance exceeding that of the ground state in any quadrature and, besides thermal noise, even for states that are not of minimal uncertainty (i.e., with $\langle X^2 \rangle \langle Y^2 \rangle > 1/16$) as those created by parametric squeezing.

In the following, we describe an experimental study of this effect and provide evidence of the realization of a nonclassical state of the macroscopic mechanical oscillator.

III. EXPERIMENTAL SETUP

A simplified scheme of the experimental setup and of the field frequencies used in the experiment is sketched in Fig. 1. The mechanical oscillator is a circular SiN membrane with a thickness of 100 nm and a diameter of 1.64 mm, equipped with a specific on-chip structure that, working as a “loss shield” [25–28], reduces the coupling between the membrane and the frame and the consequent dissipation losses. Typical quality factors are of the order of a few millions for all the membrane modes, even at low frequencies, being limited by the intrinsic dissipation in SiN.

In this work, we exploit the (0,2) drum mode at $\Omega_m/2\pi \simeq 530$ kHz, having a quality factor of 6.4×10^6 at cryogenic temperature. The membrane is placed inside a 3.92-mm-long cavity, 2 mm far from the flat back mirror, thereby forming a “membrane-in-the-middle” setup [29]. The input mirror is concave with a radius of 50 mm, which generates a waist of $70 \mu\text{m}$. The cavity linewidth is $k/2\pi = 1.9$ MHz corresponding to a finesse around 20 000. The vacuum optomechanical coupling factor is $g_0/2\pi = 30$ Hz, determined by the overlap between the membrane mechanical mode and the beam waist. The optomechanical cavity is cooled down to ≈ 7 K in an helium flux cryostat.

The light of a Nd:YAG laser is filtered by a Fabry-Perot cavity (FC) with a linewidth of 66 kHz, frequency tuned by a first acousto-optic modulator (AOM1) and then split into three

different beams. A weak probe ($\approx 20 \mu\text{W}$), phase modulated at 13.3 MHz, is kept resonant with the optomechanical cavity (OMC) using the Pound-Drever-Hall (PDH) technique with a servo loop exploiting AOM1 to correct fast fluctuations and a piezoelectric transducer to compensate slow changes of the cavity length.

About $2 \mu\text{W}$ of the reflected probe are used for the PDH locking scheme, while most of the power ($\approx 10 \mu\text{W}$) is combined with a local oscillator (LO) beam (≈ 2 mW) and sent to a balanced detection (BHD). The LO frequency ω_{LO} is blue shifted with respect to the probe (namely, by $\Delta_{\text{LO}}/2\pi = 11$ kHz) by AOM4 to realize a low-frequency heterodyne detection [30]. The BHD signal is acquired and off-line processed to study the motional sidebands and also sent to a lock-in amplifier and demodulated at frequency Ω_m . The two quadrature outputs of the lock-in amplifier are simultaneously acquired and off-line processed.

The pump beam, orthogonally polarized with respect to the probe field, consists of two tones: The main one at frequency ω_{cool} red detuned from the cavity resonance allows us to cool down the mechanical motion. The second much weaker tone at a frequency ω_{par} , blue shifted with respect to the cooling beam by $\omega_{\text{par}} - \omega_{\text{cool}} = 2\Omega_m$, realizes the parametric modulation of the oscillator generating the mechanical squeezing. The two tones are obtained by driving the AOM2 on the pump beam with the sum of two radio-frequency signals. Reference spectra in the absence of resonant parametric effects are obtained by further shifting the modulation tone by $\Delta_{\text{shift}} \approx 2\pi \times 12$ kHz. This shift is much larger than the mechanical width and much smaller than the cavity linewidth. This choice on one hand makes the coherent effect of the two tones negligible and on the other hand keeps the cooling effect of the modulation tone almost constant.

During the experiment, the frequency difference between ω_{cool} and ω_{par} is periodically changed between $2\Omega_m$ and $(2\Omega_m + \Delta_{\text{shift}})$ every 5 s. The 10-s-long time series of the BHD signal are then acquired and the 5-s segments are separated. Spectra with a resolution of 0.2 Hz are calculated from both segments and averaged over 10 consecutive time series for the subsequent analysis. In this way, we can accurately compare the spectra with and without parametric modulation

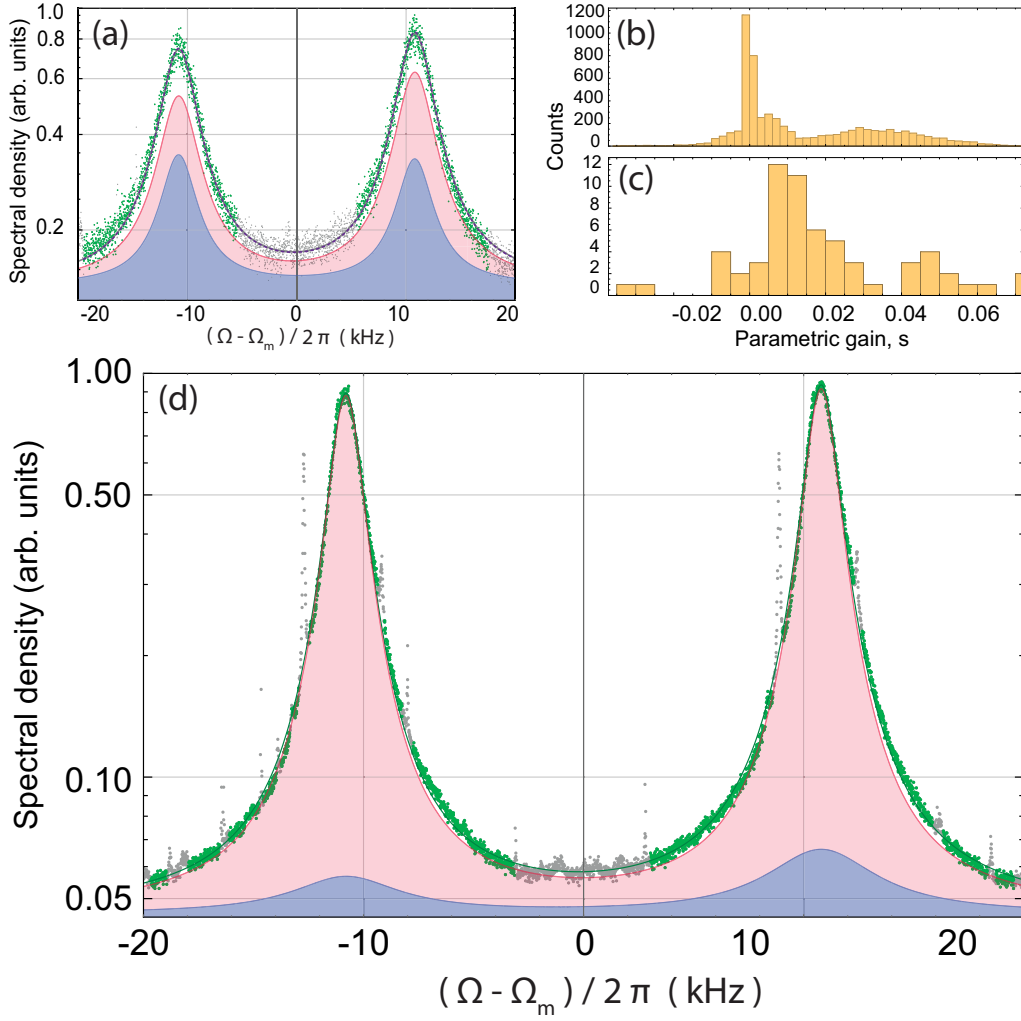


FIG. 2. [(a), (d)] Heterodyne spectra around the (0,2) drum resonance at $\Omega_m/2\pi \simeq 530$ kHz showing the two motional sidebands separated by $\Delta_{LO}/2\pi = 11$ kHz. Each experimental spectrum (green symbols) is calculated from 10, 5-s-long segments of the acquired time series. Gray symbols are used for data points excluded from the fitted regions. In panel (a), there is no resonant parametric drive, and the spectrum is fitted with one couple of Lorentzian curves (gray solid line) with equal width Γ_{eff} and different amplitudes. For the same data, we also show the fit curve with two couples of Lorentzian curves (violet dashed line) according to the expressions (30) and (31). The shaded (pink and light blue) regions shows the two Lorentzian contributions. Panel (c) shows in this case the statistical distribution for the parametric gain s , on 60 independent measurements. Panel (b) shows the statistical distribution of s obtained with the same procedure on 6000 artificial, numerically generated spectra. In panel (d) (with resonant parametric drive), the parametric gain obtained from the fit with expressions (30) and (31) (here shown with a green solid line) is $s = 0.53$.

even in the presence of slow variations in the system parameters. In order to avoid the effects of possible long-term drifts during the measurements, all the radio-frequency signals used to drive the AOMs are phase locked.

IV. EXPERIMENTAL RESULTS

As discussed in the previous sections, the analysis of the motional sidebands allows us to explore the quantum components of the mechanical squeezed dynamics. Typical heterodyne spectra, displaying the two motional sidebands centered at frequencies $\Omega_m \pm \Delta_{LO}$, are shown in Fig. 2. Without any parametric modulation [Fig. 2(a)], the spectrum consists of a couple of Lorentzian curves, having the same width Γ_{eff} but different areas. After the correction for the effect of the residual probe detuning [16], their ratio R_0 pro-

vides a direct measurement of the mean occupation number \bar{n} through $R_0 = 1 + 1/\bar{n}$. From this sideband asymmetry, we infer $\bar{n} = 5.8$ for the shown spectrum.

In the presence of parametric modulation, the oscillator quadratures are no longer identical and each sideband is composed of two Lorentzian functions centered at the same frequency but with different linewidth and amplitude. The corresponding spectra for a given parametric gain s are shown in Fig. 2(d). The spectral peaks are fitted using Eqs. (30) and (31) where, in the two widths $\Gamma_+ = \Gamma_{\text{eff}}(1 + s)$ and $\Gamma_- = \Gamma_{\text{eff}}(1 - s)$, Γ_{eff} is fixed to the value extracted from the corresponding spectra in the absence parametric drive, while the parametric gain s is left as free fitting parameter. We obtain a parametric gain of $s = 0.53 \pm 0.01$, where the quoted error corresponds to the standard deviation in five consecutive independent measurements, each one lasting 100 s. The pink

and light blue areas plotted in Fig. 2(d) show the contributions to the motional sidebands from the squeezed Y quadrature and amplified X quadrature. We remark that the shape of each sideband is no longer represented by one single Lorentzian and carries a distinctive signature of the squeezed oscillator motion.

In order to verify that the fitting procedure on the heterodyne spectra, assuming two couples of Lorentzian functions, is not biased, we have applied it to a set of 60 independent spectra acquired in the absence of parametric drive, for different values of pump power and detuning. An example of the fitted Lorentzian components is shown in Fig. 2(a) (shaded pink and light blue regions). The statistical distribution of s , displayed in Fig. 2(c), is characterized by a mean value of 0.038 and a standard deviation of 0.046, a result which is compatible with $s = 0$ as expected. The standard deviation on s is similar to those obtained in the presence of parametric drive. For a further check, we have generated artificial spectra, with $s = 0$ and the same parameters and signal-to-noise ratio of the experiment, and repeated the analysis. The statistical distribution of s derived from the fits is shown in Fig. 2(b), and displays a mean value of 0.014 and standard deviation of 0.019, figures similar to the experimental ones. It can be noticed that both the experimental and the artificial distributions are slightly asymmetric, with comparable skewness (respectively 1.12 and 0.7). This feature seems therefore related to the fitting procedure. We have not further studied this issue, but we infer that the analysis is reliable at the few hundredths level on s .

The most straightforward method to show squeezing is the direct measurement of the variance in different quadratures that are usually chosen by tuning the local oscillator phase in a homodyne detection. On the other hand, in a standard heterodyne setup, the rapidly rotating phase difference between signal and local oscillator prevents the access to selected quadratures. This drawback can be overcome by controlling such phase difference [30]. In our setup, all the oscillators are indeed phase locked, including the time base of a lock-in amplifier that demodulated the heterodyne signal at Ω_m . The spectrum of the lock-in output signal is a quadrature spectrum, centered at Δ_{LO} and symmetrized, i.e., $\frac{1}{2}[S_{X_\theta X_\theta}(\omega - \Delta_{LO}) + S_{X_\theta X_\theta}(\omega + \Delta_{LO})]$. The phase of the demodulator allows to tune θ , and thus select the Y and X quadratures. Examples of the recorded spectra are shown in Fig. 3. The quadratures spectra are acquired and analyzed independently from the heterodyne signals, and the analyses agrees for both the Lorentzian widths and the squeezing factor [21].

In the following, we describe an extended characterization of the parametric squeezing as a function of different meaningful parameters and compare the experimental results with the model reported in Sec. II.

In Fig. 4, we plot the sideband asymmetry at increasing strength of the parametric tone, keeping constant the total pump beam power, for two different values of the occupation number. When the parametric tone is not resonant (i.e., the parametric effect is off), the ratio R_0 (green symbols) remains almost constant for both occupation numbers, although we observe a clear decreasing trend as the parametric tone is increased. Such behavior is well reproduced by theoretical

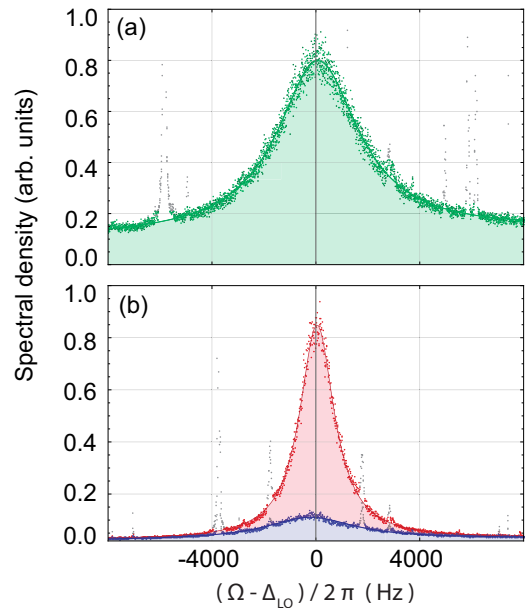


FIG. 3. Spectra of two orthogonal quadratures at the output of the lock-in amplifier. The demodulation phase is chosen to obtain respectively maximal (X) and minimal (Y) variance in the two signals, in the presence of resonant parametric modulation. (a) The parametric tone is detuned from the resonant condition. The experimental signals of the two quadratures (light and dark green symbols) are not distinguishable, and one single Lorentzian fit is shown with a solid line. (b) With resonant parametric drive, the spectra in the two quadratures (respectively red and blue symbols) are fitted with different single Lorentzian curves (red and blue solid lines). Gray symbols show spurious electronic peaks that are excluded from the fits.

curves [see Eq. (15)] calculated by using independently measured parameters, and it is due to a change in the relative strength of the two pump tones, which results in a slightly reduced cooling power. We note that the parametric effect is injected into the cavity through the pump beam and the parametric effect is turned off by shifting the driving frequency from $2\Omega_m$ to $2\Omega_m + \Delta_{\text{shift}}$ (see Sec. III). Although this procedure allows us to reduce to a minimum the changes in the cooling efficiency (as explained in Sec. III), a residual effect is still present.

Figure 4 also shows the sideband asymmetry for the Lorentzian components related to the broad quadrature R_+ (blue symbols) and narrow quadrature R_- (red symbols), with resonant parametric effect. The parametric gain s used to calibrate the horizontal axis in the figure is deduced from the width of the Lorentzian curves, as above described. The corresponding theoretical ratios can be calculated from the theoretical spectra $S_{\hat{b}^\dagger \hat{b}^\dagger}$ and $S_{\hat{b} \hat{b}}$ [Eqs. (30) and (31)] and are given by Eqs. (33) and (34). Such theoretical curves are also plotted in Fig. 4 without free fitting parameters, showing a good quantitative agreement with the experimental data.

We now analyze the sideband asymmetry as a function of the effective mechanical width Γ_{eff} , which is varied by increasing the pump power while keeping a constant mean detuning of the pump tones Δ , and parametric gain s . The experimental results and their relative theoretical curves are

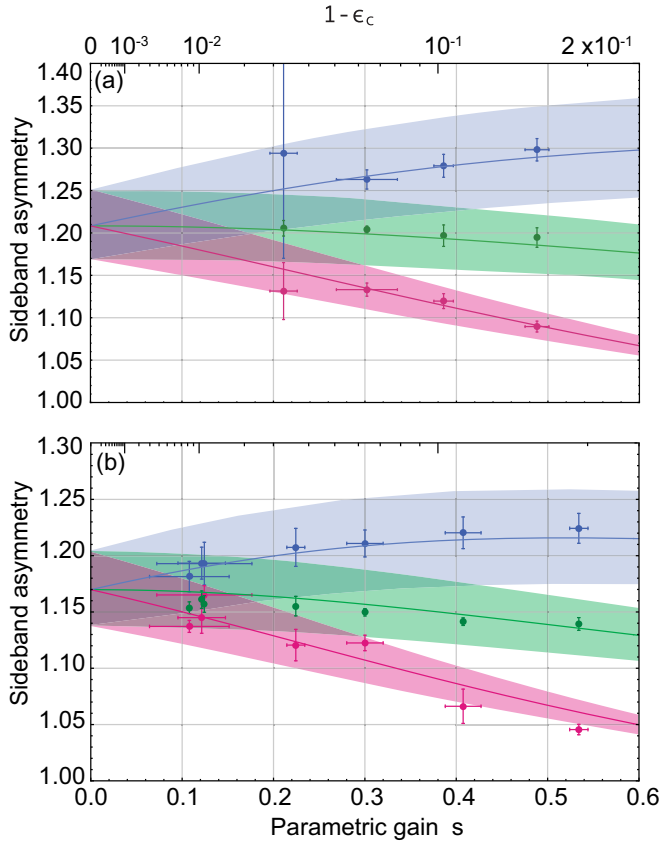


FIG. 4. Sideband asymmetry as a function of the strength of the parametric modulation (upper horizontal axis) for constant detuning and two different occupation numbers: (a) $\bar{n} = 4.2$ and (b) $\bar{n} = 5.8$. The green symbols refer to the sideband asymmetry R_0 without any resonant parametric drive, realized by detuning the modulation tone (see text). Blue (red) symbols indicate the ratio between the areas of the broad (narrow) Lorentzian contributions R_+ (R_-) in the two sidebands, observed with resonant parametric modulation. The values of parametric gain s (lower horizontal axis) are derived from the fitted widths $\Gamma_+ = \Gamma_{\text{eff}}(1 + s)$ and $\Gamma_- = \Gamma_{\text{eff}}(1 - s)$. The error bars correspond to one standard deviation calculated from five consecutive independent measurements, each one lasting 100 s. The solid lines show the corresponding theoretical behavior, with shadowed areas given by the uncertainty in the system parameters (5% in the cavity width and 0.5 K in the temperature).

displayed in Fig. 5. In the absence of any parametric modulation, R_0 increases with Γ_{eff} as expected. The mean phonon number in R_0 includes not only the cooling effect resulting from the optomechanical interaction, but also the additional occupation number due to the backaction from the probe and the pump beam. When the parametric modulation is turned on, the equivalence between R_+ and R_- is broken and the curves start to diverge, with a separation which increases with the pump power and thus with Γ_{eff} . While in the absence of parametric effect the agreement between experiment and theory is good, the data of R_+ and R_- depart from the theoretical predictions, in particular at high pump powers. We remark that the parametric gain can be written as $s = \Gamma_{\text{par}}/\Gamma_{\text{eff}}$ and thus is explicitly dependent on the mean pump detuning Δ and on the ratio between the cooling tone and total pump power

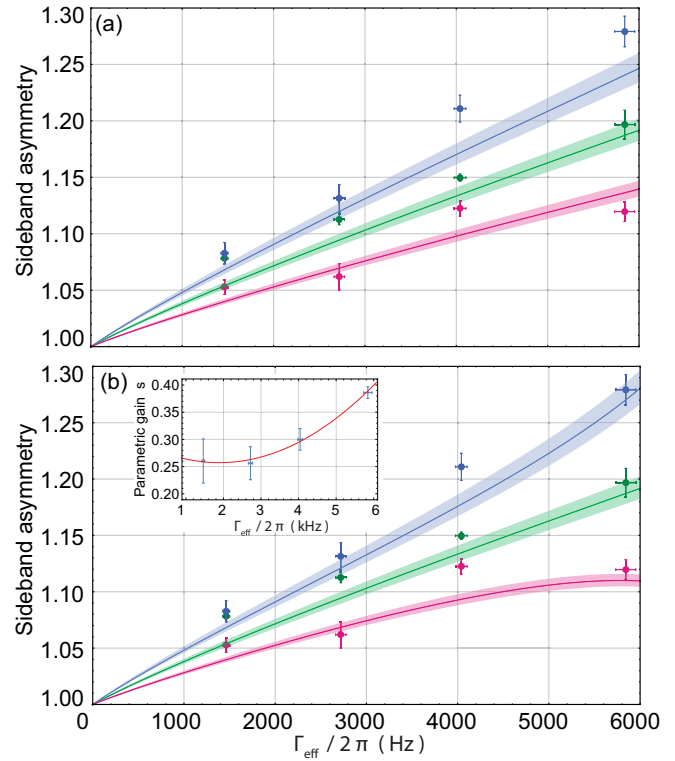


FIG. 5. (a) Sideband asymmetry as a function of Γ_{eff} for fixed mean pump detuning Δ and parametric gain s . Green symbols refer to the sideband asymmetry R_0 (without resonant parametric drive) while blue (red) symbols show ratios between the areas of the broad (narrow) Lorentzian contributions R_+ (R_-) in the presence of resonant parametric modulation. The values of Γ_{eff} in the abscissa are obtained from fits of the heterodyne spectra without resonant parametric drive. The solid lines show the corresponding theoretical behavior and shadowed areas represent the uncertainty in the system parameters (as in Fig. 3). The mean sideband asymmetry and their standard deviations are extracted from five consecutive independent measurements, each one lasting 100 s. (b) The same experimental data are compared with modified theoretical curves taking into account the changes of s with Γ_{eff} obtained by fitting the data in the inset. The χ^2 of the fit is around 0.1.

[see Eq. (17)]. During the measurements, the parametric gain is maintained roughly constant by adjusting the strength of the parametric tone each time the pump power is varied. Nevertheless, we observe a residual variation of s as shown in the inset of Fig. 5(b). We attribute such deviations to small changes of the locking point as the pump power increases, which induce changes in Δ and hence of the parametric effect. In Fig. 5(b), we show the experimental data together with modified theoretical curves for R_+ and R_- , in which we phenomenologically include the dependence of s on Γ_{eff} (see inset). These new theoretical lines show indeed a better agreement at high pump powers. However, the theory is still slightly underestimating the asymmetry at low Γ_{eff} . In this regard, we remark that the sideband asymmetry is corrected by taking into account the effect of the residual probe detuning, following the procedure described in Ref. [16]. Such corrections are typically of a few percent and become increasingly important at low Γ_{eff} , where the measured asymmetry has a

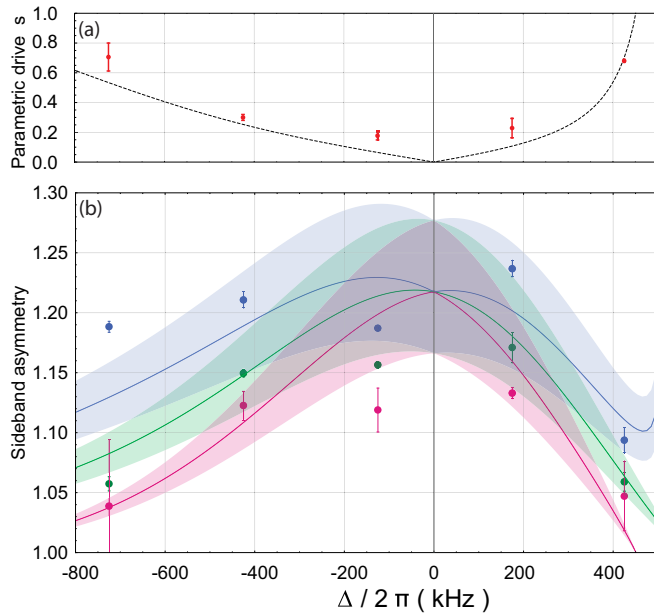


FIG. 6. (a) Parametric gain s as a function of the mean detuning of the pump tones. The experimental values of the parametric gain (red symbols) are obtained from the fitted widths $\Gamma_+ = \Gamma_{\text{eff}}(1 + s)$ and $\Gamma_- = \Gamma_{\text{eff}}(1 - s)$. The theoretical curve (dotted line) is $s = \Gamma_{\text{par}}/\Gamma_{\text{eff}}$ with Γ_{par} and Γ_{eff} given by Eqs. (17) and (15), respectively. (b) Sideband asymmetries R_0 (green), R_+ (blue), and R_- (red) as a function of the mean detuning of the pump tones Δ . The solid lines show the corresponding theoretical behavior and shadowed areas represent the uncertainty in the system parameters as in Fig. 3.

comparable magnitude. Moreover, since the data have been acquired at different times, the observed deviations could also be attributed to long-term drifts of the system parameters.

We finally study the dependence of the parametric gain and sideband asymmetry on Δ . Its variation has the twofold effect of affecting the cooling efficiency and the parametric gain. The former is evidenced by the variation of the sideband asymmetry R_0 plotted in Fig. 6(b) (green points). The corresponding theoretical curve (green line) exhibits a maximum slightly below $\Delta = 0$. $\Delta = 0$ means that the cooling tone detuning is $\omega_{\text{cool}} - \omega_c = -\Omega_m$, close to the value where optimal cooling is indeed expected. The parametric gain values are shown in Fig. 6(a), together with the theoretical curve showing a minimum equal to zero at $\Delta = 0$. The parametric gain can indeed be written as $s = \Gamma_{\text{par}}/\Gamma_{\text{eff}}$, where $\Gamma_{\text{par}} \propto \Delta$ as $\Delta \rightarrow 0$. Accordingly, as the null pump detuning is approached, the difference between the sideband ratios R_+ and R_- decreases to disappear at $\Delta = 0$ [see Fig. 6(b)].

We have seen that sideband spectra provide a powerful quantum indicator of a squeezed state: The narrow and broad Lorentzian components of each motional sideband give a signature of the imbalance between the fluctuations in the two quadratures, while the sideband asymmetry quantifies their nonclassical nature. Similarly to thermal states, even for the squeezed state the transition between classical and quantum behavior is smooth and some level of quantum squeezing is present even in macroscopic oscillators dominated by thermal noise. We remark indeed that the sideband asymmetry is in

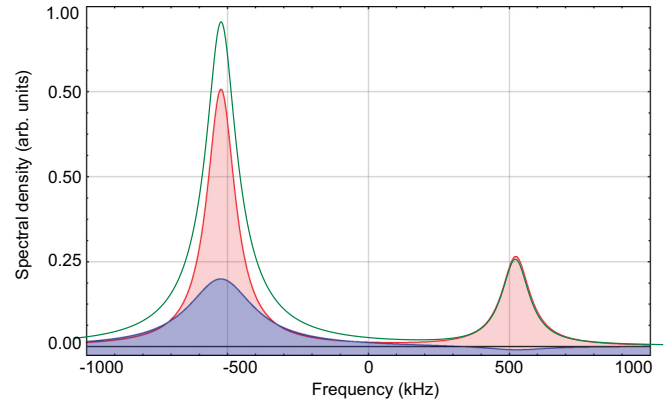


FIG. 7. Theoretical spectra of the Stokes and anti-Stokes sidebands as obtained from Eqs. (30) and (31) for $\bar{n} = 0.12$ and $s = 0.4$ (green solid line). Blue and red lines identify the broad and narrow Lorentzian components.

itself a fully quantum feature. On the other hand, it is interesting to explore the extreme case in which the residual fluctuations in the squeezed quadrature are reduced below the zero-point level. This occurs for $(2\bar{n} + 1)/(1 + s) < 1$, i.e., for $s > 2\bar{n}$. Equation (31) dictates that the broad Lorentzian contribution to the anti-Stokes sideband becomes negative, although this is overcompensated for by the narrow component, as the overall spectral density obviously remains positive at all frequencies. A spectrum with these characteristics is illustrated in Fig. 7. The negativity of the broad component in the anti-Stokes sideband provides a clear indication of a *bona fide* quantum squeezing without the necessity of absolute calibrations. Under a continuous parametric drive, the system is stable for $s < 1$, which represents the parametric instability threshold. The condition $s > 2\bar{n}$ would then require an initial occupation number $\bar{n} < 0.5$, a level that has already been reached even in optomechanical setups based on SiN membranes (see, e.g., Refs. [4,31]).

V. CONCLUSIONS

We have recently described a cavity optomechanics experiment where a macroscopic mechanical oscillator is parametrically driven by a suitable combination of optical fields [21]. We have shown that the generated mechanical squeezed state exhibits a quantum dynamics that is evidenced by the shape of the motional sidebands. In the present work, we describe the theoretical model behind this phenomenon and present a detailed characterization of the experimental achievements in good agreement with the model. We suggest that the analysis of the motional sidebands can provide a clear signature of the noise reduction below the zero-point fluctuations that occurs in one quadrature, without requiring any absolute calibration of the displacement spectra or even a direct measurement of the quadrature fluctuations.

Our results widen the range of macroscopic nonclassical states that can be explored in optomechanical experiments. For instance, interesting developments can involve nonstationary squeezed states and multimode squeezing [32–34].

ACKNOWLEDGMENTS

Research was performed within the Project QuaSeRT funded by the QuantERA ERA-NET Cofund in Quantum Technologies implemented within the European Union's Horizon 2020 Programme. The research has been partially supported by INFN (HUMOR project).

-
- [1] M. Aspelmeyer, T. J. Kippenberg, and F. Marquardt, *Rev. Mod. Phys.* **86**, 1391 (2014).
- [2] S. M. Meenehan, J. D. Cohen, G. S. MacCabe, F. Marsili, M. D. Shaw, and O. Painter, *Phys. Rev. X* **5**, 041002 (2015).
- [3] R. Riedinger, S. Hong, R. A. Norte, J. A. Slater, J. Shang, A. G. Krause, V. Anant, M. Aspelmeyer, and S. Gröblacher, *Nature (London)* **530**, 313 (2016).
- [4] R. W. Peterson, T. P. Purdy, N. S. Kampel, R. W. Andrews, P. L. Yu, K. W. Lehnert, and C. A. Regal, *Phys. Rev. Lett.* **116**, 063601 (2016).
- [5] A. H. Safavi-Naeini, J. Chan, J. T. Hill, T. P. M. Alegre, A. Krause, and O. Painter, *Phys. Rev. Lett.* **108**, 033602 (2012).
- [6] T. P. Purdy, P. L. Yu, N. S. Kampel, R. W. Peterson, K. Cicak, R. W. Simmonds, and C. A. Regal, *Phys. Rev. A* **92**, 031802(R) (2015).
- [7] M. Underwood, D. Mason, D. Lee, H. Xu, L. Jiang, A. B. Shkarin, K. Børkje, S. M. Girvin, and J. G. E. Harris, *Phys. Rev. A* **92**, 061801(R) (2015).
- [8] V. Sudhir, D. J. Wilson, R. Schilling, H. Schutz, S. A. Fedorov, A. H. Ghadimi, A. Nunnenkamp, and T. J. Kippenberg, *Phys. Rev. X* **7**, 011001 (2017).
- [9] L. Qiu, I. Shomroni, M. A. Ioannou, N. Piro, D. Malz, A. Nunnenkamp, and T. J. Kippenberg, *Phys. Rev. A* **100**, 053852 (2019).
- [10] L. Qiu, I. Shomroni, P. Seidler, and T. J. Kippenberg, *Phys. Rev. Lett.* **124**, 173601 (2020).
- [11] F. Y. Khalili, H. Miao, H. Yang, A. H. Safavi-Naeini, O. Painter, and Y. Chen, *Phys. Rev. A* **86**, 033840 (2012).
- [12] A. J. Weinstein, C. U. Lei, E. E. Wollman, J. Suh, A. Metelmann, A. A. Clerk, and K. C. Schwab, *Phys. Rev. X* **4**, 041003 (2014).
- [13] K. Børkje, *Phys. Rev. A* **94**, 043816 (2016).
- [14] T. P. Purdy, K. E. Grutter, K. Srinivasan, and J. M. Taylor, *Science* **356**, 1265 (2017).
- [15] V. Sudhir, R. Schilling, S. A. Fedorov, H. Schütz, D. J. Wilson, and T. J. Kippenberg, *Phys. Rev. X* **7**, 031055 (2017).
- [16] A. Chowdhury *et al.*, *Quantum Sci. Technol.* **4**, 024007 (2019).
- [17] E. E. Wollman *et al.*, *Science* **349**, 952 (2015).
- [18] J. M. Pirkkalainen, E. Damskagg, M. Brandt, F. Massel, and M. A. Sillanpaa, *Phys. Rev. Lett.* **115**, 243601 (2015).
- [19] F. Lecocq, J. B. Clark, R. W. Simmonds, J. Aumentado, and J. D. Teufel, *Phys. Rev. X* **5**, 041037 (2015).
- [20] C. U. Lei, A. J. Weinstein, J. Suh, E. E. Wollman, A. Kronwald, F. Marquardt, A. A. Clerk, and K. C. Schwab, *Phys. Rev. Lett.* **117**, 100801 (2016).
- [21] A. Chowdhury, P. Vezio, M. Bonaldi, A. Borrielli, F. Marino, B. Morana, G. A. Prodi, P. M. Sarro, E. Serra, and F. Marin, *Phys. Rev. Lett.* **124**, 023601 (2020).
- [22] D. Rugar and P. Grütter, *Phys. Rev. Lett.* **67**, 699 (1991).
- [23] A. Pontin, M. Bonaldi, A. Borrielli, F. S. Cataliotti, F. Marino, G. A. Prodi, E. Serra, and F. Marin, *Phys. Rev. Lett.* **112**, 023601 (2014).
- [24] S. Sonar, V. Fedoseev, M. J. Weaver, F. Luna, E. Vlieg, H. van der Meer, D. Bouwmeester, and W. Löffler, *Phys. Rev. A* **98**, 013804 (2018).
- [25] A. Borrielli *et al.*, *Microsyst. Technol.* **20**, 907 (2014).
- [26] A. Borrielli *et al.*, *Phys. Rev. B* **94**, 121403(R) (2016).
- [27] E. Serra *et al.*, *AIP Adv.* **6**, 065004 (2016).
- [28] E. Serra, B. Morana, A. Borrielli, F. Marin, G. Pandraud, A. Pontin, G. A. Prodi, P. M. Sarro, and M. Bonaldi, *J. Microelectromech. Syst.* **27**, 1193 (2018).
- [29] A. M. Jayich, J. C. Sankey, B. M. Zwickl, C. Yang, J. D. Thompson, C. A. A. Girvin, F. Marquardt, and J. G. E. Harris, *New J. Phys.* **10**, 095008 (2008).
- [30] A. Pontin, J. E. Lang, A. Chowdhury, P. Vezio, F. Marino, B. Morana, E. Serra, F. Marin, and T. S. Monteiro, *Phys. Rev. Lett.* **120**, 020503 (2018).
- [31] I. Galinskiy, Y. Tsaturyan, M. Parniak, and E. S. Polzik, *Optica* **7**, 718 (2020).
- [32] I. Mahboob, H. Okamoto, K. Onomitsu, and H. Yamaguchi, *Phys. Rev. Lett.* **113**, 167203 (2014).
- [33] Y. S. Patil, S. Chakram, L. Chang, and M. Vengalattore, *Phys. Rev. Lett.* **115**, 017202 (2015).
- [34] A. Pontin *et al.*, *Phys. Rev. Lett.* **116**, 103601 (2016).